Ultrasonics Sonochemistry 89 (2022) 106161

Contents lists available at ScienceDirect

Ultrasonics Sonochemistry

journal homepage: www.elsevier.com/locate/ultson

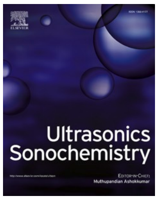

Residue-free acoustofluidic manipulation of microparticles via removal of microchannel anechoic corner

Muhammad Soban Khan [a], Mehmet Akif Sahin [b], Ghulam Destgeer [b,**], Jinsoo Park [a,*]

[a] *Department of Mechanical Engineering, Chonnam National University, 77 Yongbong-ro, Buk-gu, Gwangju 61186, Republic of Korea*
[b] *Control and Manipulation of Microscale Living Objects, Central Institute for Translational Cancer Research (TranslaTUM), Department of Electrical and Computer Engineering, Technical University of Munich, Einsteinstraße 25, Munich 81675, Germany*

ARTICLE INFO

Keywords:
Surface acoustic wave
Acoustofluidics
Microchannel anechoic corner
Particle manipulation
Thermal reflow

ABSTRACT

Surface acoustic wave (SAW)-based acoustofluidics has shown significant promise to manipulate micro/nano-scale objects for biomedical applications, e.g. cell separation, enrichment, and sorting. A majority of the acoustofluidic devices utilize microchannels with rectangular cross-section where the acoustic waves propagate in the direction perpendicular to the sample flow. A region with weak acoustic wave intensity, termed microchannel anechoic corner (MAC), is formed inside a rectangular microchannel of the acoustofluidic devices where the ultrasonic waves refract into the fluid at the Rayleigh angle with respect to the normal to the substrate. Due to the absence of a strong acoustic field within the MAC, the microparticles flowing adjacent to the microchannel wall remain unaffected by a direct SAW-induced acoustic radiation force (ARF). Moreover, an acoustic streaming flow (ASF) vortex produced within the MAC pulls the particles further into the corner and away from the direct ARF influence. Therefore, a residue of particles continues to flow past the SAWs without intended deflection, causing a decrease in microparticle manipulation efficiency. In this work, we introduce a cross-type acoustofluidic device composed of a half-circular microchannel, fabricated through a thermal reflow of a positive photoresist mold, to overcome the limitations associated with rectangular microchannels, prone to the MAC formation. We investigated the effects of different microchannel cross-sectional shapes with varying contact angles on the microparticle deflection in a continuous flow and found three distinct regimes of particle deflection. By systematically removing the MAC out of the microchannel cross-section, we achieved residue-free acoustofluidic microparticle manipulation via SAW-induced ARF inside a half-circular microchannel. The proposed method was applied to efficient fluorescent coating of the microparticles in a size-selective manner without any residue particles left undeflected in the MAC.

1. Introduction

Ultrasonic surface acoustic wave (SAW)-driven microfluidics has experienced an unprecedented growth over the last decade for precise control of microfluidic flows and micro/nano-objects [1–3], examples of which are manipulation of micro/nano-particles [4–6], cells [7], droplet [8,9], biomolecules [10,11], microorganisms [7,12], and mixing [13–15], pumping [16,17], and atomization [18,19] of the fluids. In SAW-based acoustofluidic devices, SAWs are produced from an interdigital transducer (IDT) patterned on a piezoelectric substrate due to the inverse-piezoelectric effect when an alternating current (AC) signal with a resonant frequency is applied to the IDT. Most acoustofluidic devices operate in a cross-type arrangement, in which the Rayleigh-type SAWs propagate perpendicular to the flow direction [1,20,21]. When the SAWs meet the fluid inside the microchannel, they refract into the microchannel in the form of longitudinal waves (LWs) at the Rayleigh angle (θ_R) determined by the Snell's law. Due to the right incident angle and the θ_R with respect to the normal to the substrate, a microchannel anechoic corner (MAC) void of a noticeable acoustic field is formed inside the microchannel [5,22]. When microspheres, whose diameter comparable to or larger than the acoustic wavelength divided by pi, suspended in fluid are exposed to progressive LWs, they scatter the LWs in an anisotropic manner (Mie or Geometrical scattering) and, as a consequence, they experience an acoustic radiation force (ARF) in the

---

* Corresponding author.
** Co-corresponding author.
E-mail addresses: ghulam.destgeer@tum.de (G. Destgeer), jinsoopark@jnu.ac.kr (J. Park).

https://doi.org/10.1016/j.ultsonch.2022.106161
Received 15 May 2022; Received in revised form 18 August 2022; Accepted 3 September 2022

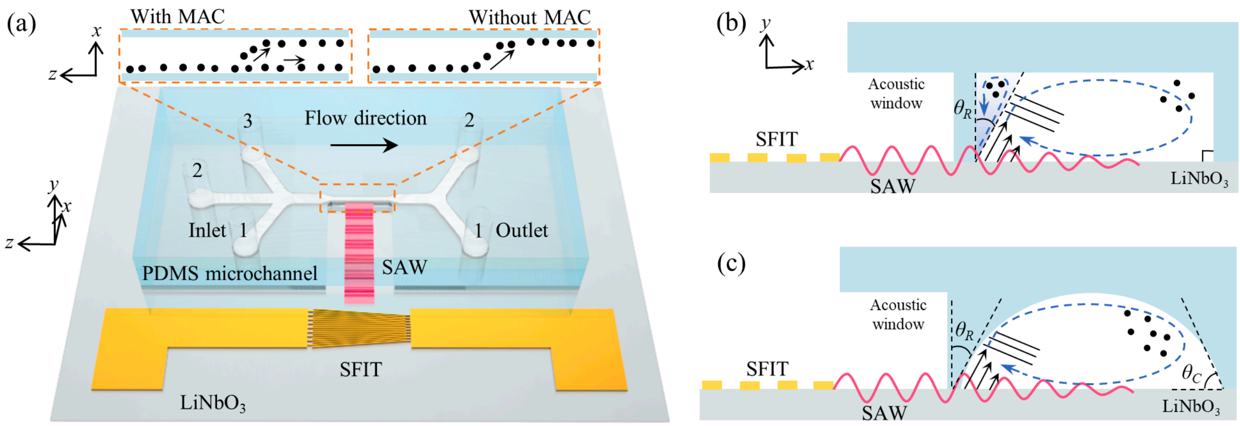

Fig. 1. (a) Schematic diagram of an acoustofluidic device with insets indicating particle deflection inside a microchannel with or without microchannel anechoic corner (MAC). Cross sectional-views of (b) rectangular and (c) half-circular microchannels in the acoustofluidic devices.

wave propagation direction. For acoustofluidic microparticle manipulation, the travelling SAW-induced acoustic ARF offers high-resolution, size-selective control of the microparticles with improved deflection distance, compared to the standing SAW-induced ARF [1,23]. In acoustofluidic applications, where microparticles should be manipulated, the particles present within the MAC region do not experience the SAW-induced ARF and thus remain as residue particles within the corner region, resulting in decreased microparticle recovery rate [5,22]. Many previous devices introduced a sheath fluid flow to shift the microparticles away from the MAC region, and the requirement of the additional flow into the device leads to the increased complexity of the device configuration and operation [24–26].

In this research, we propose a cross-type acoustofluidic device composed of a slanted finger interdigital transducer (SFIT) deposited on a piezoelectric substrate and a half-circular microchannel for removal of the MAC region toward residue-free microparticle manipulation via SAW-induced ARF. The half-circular microchannel can be fabricated through thermal reflow of a positive photoresist (PR) mold. During the thermal reflow process, a rectangular PR microstructure patterned by a photolithography process transforms into a PR microstructure with filleted corners, which serves as a mold for the half-circular polydimethylsiloxane (PDMS) microchannel. We controlled the thermal reflow conditions and fabricated half-circular microchannels with varying contact angle (θ_C) to investigate its effects on the acoustic pressure field formed within the microchannel, acoustic streaming flow profile, and resulting microparticle manipulation. We found three different regimes of particle deflection depending on the existence of the residue particles and the standing wave formation, as will be delineated. We applied the findings to the residue-free microparticle manipulation via SAW-induced ARF in a half-circular microchannel with optimized θ_C. Moreover, we utilized the proposed acoustofluidic device for residue-free, size-selective fluorescent coating of the microparticles left in the microchannel in a continuous, contactless, and label-free manner.

2. Methodology

2.1. Device configuration and working principle

Fig. 1(a) shows a schematic diagram for the proposed cross-type acoustofluidic device that comprises an SFIT deposited on a piezoelectric lithium niobate (LiNbO$_3$) substrate and a PDMS microchannel on top of the substrate. The SFIT, with variable electrode width and spacing, has a wide resonant frequency bandwidth to produce SAWs with a range of different frequencies, instead of a single resonant frequency. When actuated by a high-frequency AC signal, the corresponding region of the SFIT resonates and thus generates SAWs with the applied frequency. It should be noted that the SFIT is utilized for flexible modulation of the working frequency. A simple IDT with uniform electrode width could also be used instead as in our earlier studies [26–28]. The PDMS microchannel has an acoustic window in the form of an air cavity on the SFIT side to prevent significant absorption of the acoustic waves within PDMS walls before acoustic coupling with the fluid inside the microchannel. The SAWs propagate through the acoustic window in the perpendicular direction to the flow and interact with the fluid confined within the microchannel. Most of the previous SAW-driven acoustofluidic devices adopted the rectangular microchannel, as shown in Fig. 1(b). The SAWs with a right incident angle refract into the microchannel in the form of LWs at the Rayleigh angle θ_R, which is determined by Snell's law as $\theta_R = \sin^{-1}(c_f/c_s)$ where c_f and c_s are the speeds of sound in the fluid and on the substrate, respectively. As a result, the MAC region with an acute triangular shape is formed at the top-corner near the SFIT within the microchannel, as shown in Fig. 1(b). When the microparticles are exposed to the SAW-induced acoustic field, most microparticles are translocated in the SAW propagation direction by the ARF because of the anisotropic wave scattering off the spherical microparticles. However, the particles suspended close to the wall in the MAC region remain unaffected by the SAW-induced ARF as residual microparticles because the acoustic pressure fluctuations are deficient in the MAC region while the smaller acoustic streaming flow (ASF) vortex further pulls the particles into the MAC region. On the other hand, the half-circular microchannel in Fig. 1(c) can be used to remove the MAC region to circumvent any limitations caused by the MAC effect in the cross-type acoustofluidic devices. The half-circular microchannel can be fabricated by using thermal reflow of positive PR, which will be delineated in a subsequent section. As easily inferred, the contact angle θ_C of the half-circular microchannel at both sides should desirably be the difference between the right angle and the θ_R such that $\theta_C = 90^\circ - \theta_R$ to prevent the MAC region from being formed. Under the condition where $\theta_C \cong 90^\circ - \theta_R$, the refracting LWs propagate throughout the whole microchannel without forming the MAC region and a counter clockwise ASF vortex, as in the case of the rectangular microchannels. As a result, the microparticles located anywhere in the microchannel experience the SAW-induced ARF, and they are deflected in the wave propagation direction without any residual microparticles left close the wall near the SFIT [22].

2.2. Fabrication of half-circular microchannel using positive photoresist thermal reflow

Thermal reflow refers to the displacement or relocation of a material driven by surface tension above a certain threshold temperature. During the thermal reflow of thermoplastic materials, an initial structure is reshaped as the material is allowed to flow at increased temperature above the glass transition temperature. This morphological transformation process can be controlled by various conditions such as

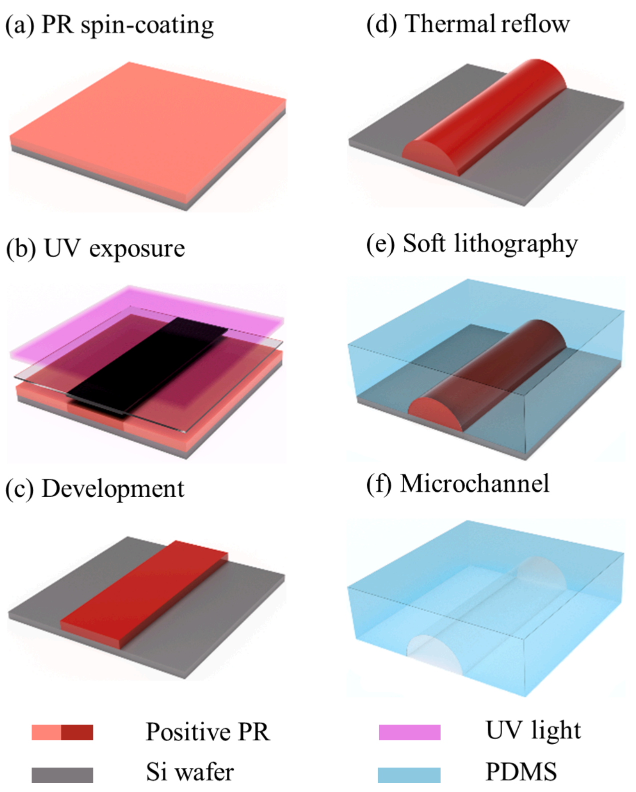

Fig. 2. Thermal reflow assisted soft lithography process to fabricate a half-circular PDMS microchannel by using positive photoresist (PR) replica mold.

thermal reflow temperature, molecular weight, polymer dispersity, viscosity, and time [29]. In PR thermal reflow, an original microstructure with a rectangular cross-section obtained by a conventional photolithography can be transformed into a surface energy-optimized microstructure with a half-circular cross-section. The photo-sensitive polymer is solidified after cooling at room temperature to preserve the modified morphology. Unlike linear thermoplastic materials, typical positive PR reflows above the critical temperature of approximately 110–130 °C, begins to harden beyond 130 °C because of the interaction with the ambient oxygen and starts to cross-link with increased adhesion above 140 °C [29]. Fig. 2 represents the fabrication process of the half-circular PDMS microchannel by using the thermal reflow of the positive PR microstructure obtained by a typical photolithography process. First, a thin PR layer is spin-coat with a desirable thickness on a Si wafer (Fig. 2(a)). After the pre-baking at 120 °C for 10 min and UV exposure, the PR exposed to the UV light becomes soluble in a developer solution as the applied UV energy dissociates the sensitizer and breaks down the cross-links (Fig. 2(b)). When developed, the exposed PR dissolves while the unexposed PR remains (Fig. 2(c)). The rectangular cross-section of the fabricated microstructure with vertical sidewalls are thermally transformed into the lens-like half-circular cross-section by thermal treatment at 130 °C for 2 min and 30 sec, followed by cooling at room temperature (Fig. 2(d)). After surface silanization, the 10:1 ratio PDMS mixture was poured into the PR master mold and cured in a 65 °C for 12 h (Fig. 2(e)). The cured PDMS replica was gently peeled off from the mold to finally obtain the half-circular microchannel (Fig. 2(f)).

3. Experimental

On a 500 µm-thick 128°-rotated Y-cut X-propagating $LiNbO_3$ wafer (MTI Korea), a pair of slanted-finger electrodes composed of a bimetallic layer of Cr and Au (thickness of 20 and 100 nm, respectively) were deposited to form an SFIT by photolithography, E-beam evaporation, and lift-off processes [30]. The SFIT used in the experiments had varying electrode width and spacing (λ/4) of 7–9 µm, metal ratio of 0.5, a total aperture of 1000 µm, and 40 finger pairs. The corresponding resonant frequency bandwidth of the SFIT was measured to be 110–138 MHz by a vector network analyzer (E5071B, Agilent Technologies). An RF signal generator (BSG F10, Belektronig GmbH) was used to provide an AC signal to the SFIT and monitor the transducer actuation. The rectangular and half-circular microchannel molds were fabricated with a positive PR (ma-P 1275 HV, micro resist technology GmbH) on a Si wafer by a

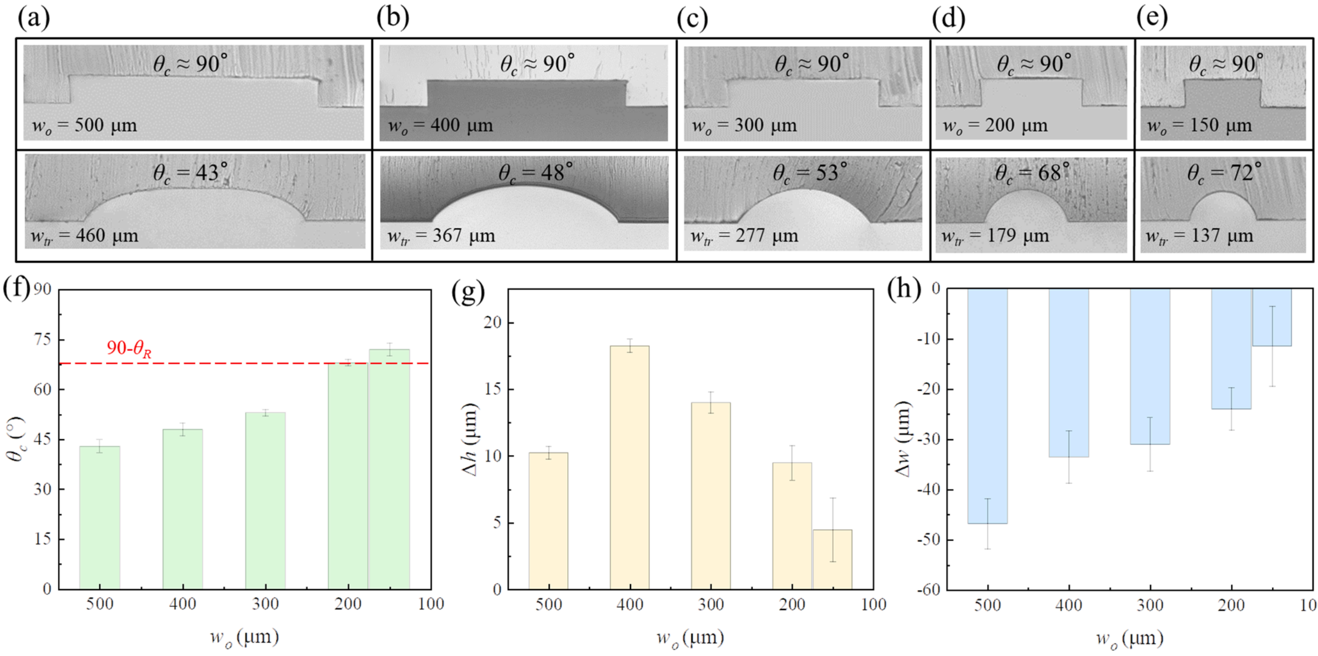

Fig. 3. (a–e) The cross-sectional view of the microchannel before (top) and after the thermal reflow (bottom), respectively. (f) The contact angles θ_C after thermal reflow are plotted opposite to the initial widths (w_O) of rectangular channels. A horizontal dashed line marks a critical θ_C value with respect to the Rayleigh angle θ_R = 22°. Similarly, change in microchannel height Δh (g) and width Δw (h) with respect to the initial dimensions of rectangular channels are plotted against w_O after thermal reflow.

typical photolithography process with corresponding developer (ma-D 331, micro resist technology GmbH). The PDMS mixture (Sylgard 184A and 184B, Dow Corning), with a weight ratio of 10:1 for the base and curing agent, was poured onto the 1H, 1H, 2H, 2H-Perfluorooctyltriethoxysilane (Sigma-Aldrich)-treated PR mold to fabricate the PDMS microchannels. The resulting microchannels were then irreversibly bonded to the $LiNbO_3$ substrate by oxygen plasma treatment (Covance, Femto Science). The height (h) and width (w) of the rectangular microchannel were 57 μm and 150–500 μm, respectively, whereas the height, width, and the θ_C of the half-circular microchannels varied as h = 59–73 μm, w = 143–464 μm, and θ_C = 43–72° due to the morphological change depending on the thermal reflow conditions. Fluorescent polystyrene (PS) microspheres (Thermo Scientific, Inc.) with diameters of 5 and 6 μm were used as model particles. The PS microparticles, suspended in deionized water (Dyne Bio Inc.) with 5 wt% of TWEEN® 20 (Sigma-Aldrich), were injected into the microchannels using a syringe pump (neMESYS Cetoni GmbH). The microparticle behaviors were observed under a fluorescent inverted microscope (IX73, Olympus) equipped with a high-speed CMOS camera (VEO 710L, Phantom) and a CCD camera (E3ISPM, RisingCam). For size-selective fluorescent coating application, negatively charged red fluorescent 6 μm PS microsphere (Micromod, Inc.) were coated with positively charged poly(fluorescein isothiocyanate allylamine hydrochloride) (PAH-FITC) (Sigma-Aldrich). The PAH-FITC solution at 0.1 mg/mL was used to make a fluorescently labeled polyelectrolyte solution for the coating experiment whereas negatively charged green fluorescent 5 μm PS microsphere (Thermo Scientific, Inc.) remained uncoated with the help of size-selective acoustofluidic particle separation.

4. Results and discussion

4.1. Characterization of half-circular microchannel fabrication by thermal reflow

Using the thermal reflow method, the microchannels were created with varying contact angle θ_C, allowing us to investigate the MAC formation. Five different PR molds having rectangular cross-section with original widths of w_o = 150, 200, 300, 400 and 500 μm were considered to study the θ_C modulation induced by thermal reflow. A batch of the rectangular microchannels with different widths were fabricated using a conventional soft lithography process. Another batch of half-circular microchannels were fabricated from the half-circular PR molds, produced by heating the rectangular molds for thermal reflow. Thermal reflow requires 10s of minutes to complete, during which the structure's height increases in the first few minutes and then decreases over time [29]. Usually, this PR thermal reflow approach is used to fabricate structures with small contact angle of $\theta_C \sim$ 20–40° and shallow height. On the contrary, in this study, we intentionally heated the rectangular PR molds during a comparably short period of time to acquire the microchannels with $40^\circ < \theta_C < 90^\circ$. For this purpose, the thermal reflow conditions were optimized as 130 °C for around 2 min and 30 sec. This short-term thermal reflow approach allowed us to tune the contact angle θ_C of the half-circular microchannel to be comparable to $68^\circ = 90^\circ - \theta_R$ for efficient residue-free acoustofluidic manipulation of microparticles.

Table 1
Material and wave properties used in simulation.

	$LiNbO_3$	Water
Speed of sound, c [m/s]	3950	1482
Density, ρ [kg/m^3]	4620	1000
Dynamic viscosity, μ [mPa.s]		1.002
Bulk viscosity, μ^b [mPa.s]		2.7765
Attenuation coefficient, α [1/m]	2421	
Attenuation coefficient, β [1/m]	690	
Wavelength, λ [μm]	33.5	
Amplitude of wave [nm]	0.1	

Fig. 3(a–e) depicts the cross-sectional microscopic images of the fabricated rectangular microchannels (top) and half-circular microchannels after thermal reflow (bottom). We discovered that the width of the PR mold is closely related to the morphological change after the thermal reflow process. The changes in θ_C, height ($\Delta h = h_{tr} - h_o$), and width ($\Delta w = w_{tr} - w_o$), where the subscripts o and tr indicate the values before and after the thermal reflow, of the half-circular microchannels with reference to those of the rectangular microchannel are plotted as a function of the original width of the rectangular PR mold in Fig. 3(f–h), respectively. Fig. 3(f) demonstrates that as a result of the thermal reflow process θ_C decreased from 90° to 43° for a 500 μm wide channel – a fall of 47°. However, for a 150 μm wide channel, θ_C decreased only by 18° to $\theta_C \approx 72^\circ$. Hence, an increasing trend for θ_C in the half-circular PR molds after thermal reflow was observed for decreasing channel width. Moreover, after thermal reflow, as the height of microchannel increased ($\Delta h > 0$), the width decreased ($\Delta w > 0$) with respect to the initial dimensions of the rectangular microchannel (Fig. 3(g and h)). The most significant change in height Δh was observed at ~17 μm for w_o = 400 μm with decreasing trend with decreasing in w_o except the case of w_o = 500 μm. The exceptional case can be attributed to the inhomogeneous curvature in the bottom of Fig. 3(a). The trend suggests that for the given initial height (i.e. ~57 μm) of the PR structure, the Δh would decrease further for both wider or narrower channels after peaking at w_0 = 400 μm, which can be explained by the surface energy of the molten PR, aspect ratio (AR = w_o/h_o) of the structure, and available volume to reflow. For the former case with a large volume to reconfigure itself (i.e. $w_o \geq 500$ μm, AR ≥ 8.8), the thermal reflow would affect significantly at the edges of the structure minimizing the surface energy, whereas the middle part would be least deformed with insignificant change in height. For the latter case (i.e. $w_o \leq 150$ μm, AR ≤ 2.6), the smaller structure volume and surface energy of the molten PR would prevent it from deforming away from a semi-circular shape. The width of the channels decreased for all the cases as the rectangular cross-sections transformed into a low-energy circular-cap shape. The most significant change in Δw was found for 500 μm wide channels at approximately −47 μm, which could be further prominent for wider channels. For w_o = 150 μm, the smallest change was found in our experiments at $\Delta w \sim -11$ μm.

4.2. Numerical simulation of acoustic pressure and streaming velocity fields

COMSOL Multiphysics was used to estimate the direction and propagation of SAWs. Acoustic waves attenuated at the substrate-fluid interface and within the viscous fluid with attenuation coefficients of α and β, respectively. The acoustic waves upon coupling with the fluid are radiated inside the microchannel with θ_R , reflected from the top wall and propagated towards the right wall. Attenuation coefficients, α and β, are given by [31].

$$\alpha = \frac{\rho_f c_f}{\rho_s c_s \lambda_f}$$

$$\beta = \frac{\omega^2}{\rho_f c_f \lambda_f}\left(\frac{4}{3}\mu + \mu^b\right) \tag{1}$$

where ρ is density, c is speed of sound with subscripts f and s for fluid and substrate, ω is the angular frequency, and μ and μ^b are dynamic and bulk viscosities of fluid, respectively. The acoustic pressure distribution inside the PDMS microchannels was simulated for rectangular and half-circular cross sections. The fluid domain (water) was excited by an oscillating velocity boundary condition, $v(x, t|y = 0)$, along the bottom wall of microchannel modelled as a replacement of the SAW propagation. Both types of microchannels were encompassed by PDMS walls and modelled as impedance boundary condition $Z_{PDMS} = \rho_{PDMS}\, c_{PDMS}$. The wave velocity along substrate surface was defined by decaying and oscillatory functions and written as [32].

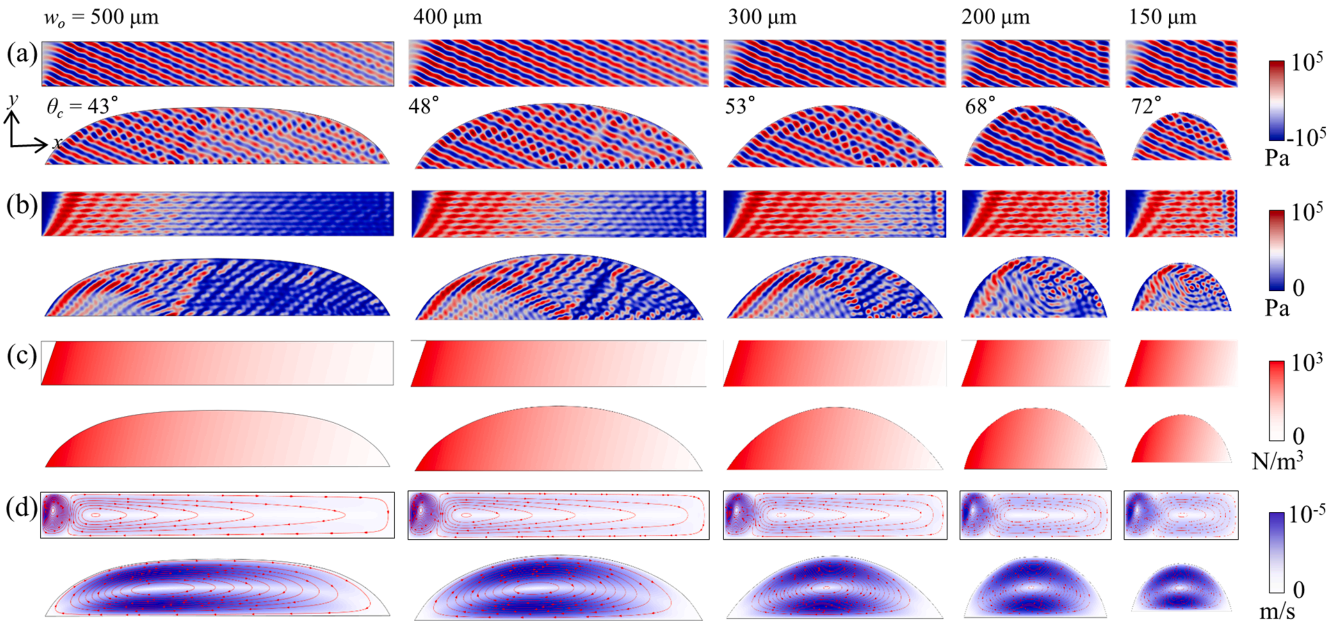

Fig. 4. First-order total pressure (a), time-averaged absolute pressure (b), implemented body force (c), and acoustic streaming flow velocity (d) due to viscous damping of acoustic waves (f = 117 MHz) are plotted for rectangular (top) and half-circular (bottom) microchannels depicted in Fig. 3(a).

$$v_x(x,t\,|y=0) = 0.86u_0\omega e^{-\alpha x}\sin\left(\frac{2\pi x}{\lambda_f}-\omega t\right)$$

$$v_y(x,t|y=0) = u_0\omega e^{-\alpha x}sin\left(\frac{2\pi x}{\lambda_f}-\omega t\right) \qquad (2)$$

where u_0 is the amplitude of the wave (assumed 0.1 nm as reported earlier [33]) decreasing exponentially in the x-direction with the attenuation coefficient α. The parameter values used for numerical simulations are summarized in Table 1. Fig. 4(a-b) shows the first-order and absolute time-averaged acoustic pressure distribution for rectangular and half-circular cross sections, respectively. These simulations confirm the removal of MAC, i.e. the region with a minimal acoustic field presence, in the half-circular channels, which is depicted very clearly in the rectangular channels. The total acoustic pressure plots indicate travelling LWs propagating inside the microchannel, whereas the time-averaged absolute pressure plots highlight highest and lowest acoustic pressure regions. The lowest acoustic pressure region within rectangular channels matches very well with the proposed MAC regions.

The travelling LWs propagating through a fluid medium attenuates due to viscous damping and results in an ASF in the Eckart streaming mode, which has been extensively utilized for acoustofluidic flow control [13,15]. Viscous damping of acoustic waves can be described by a body force in numerical models solving Navier-Stokes equation. A single SFIT-based actuation of the fluid by SAWs and absence of strong standing waves formation due to low reflection of travelling LWs off PDMS walls to result in a momentum flux or a body force in the direction of wave attenuation. This body force can be described as [34]:

$$\vec{F} = \rho_f\langle\vec{v_1}.\nabla\vec{v_1}\rangle + \rho_f\langle\vec{v_1}\nabla.\vec{v_1}\rangle \qquad (3)$$

where $\vec{v_1}$ is the first-order acoustic sound velocity and the brackets $\langle\cdots\rangle$ imply a time-averaged operation. Siebert et al. [33] derived an improved description for body forces using Eq. (3) where the experimental results were more accurately in line with the simulated fluid streaming. This simplified body force representation is:

$$\vec{F} = \rho_f\omega^2u_0e^{\left(-2\left(b_xx+b_yy\right)\right)}\frac{\left(\vec{b}\vec{b}\bullet\vec{b}-\vec{k}\vec{b}\bullet\vec{k}\right)}{\left(-\vec{b}+\vec{k}\right)^2} \qquad (4)$$

where $\vec{k}$ and $\vec{b}$ is real and imaginary part of the complex wave vector, respectively. Eq. (4) was implemented in the numerical model to solve Navier-Stokes equation under laminar flow assumption. The body force was implemented with respect to the Rayleigh angle θ_R (estimated by Snell's law as ∼22°), where the MAC region was intentionally excluded from the body force domain (Fig. 4(c)). For rectangular channels, a triangular MAC region was excluded based on θ_R, whereas for half-circular channels, the MAC region was already absent. As the body force decayed in the x and y-directions, ASF vortices were produced (Fig. 4(d)). For the rectangular channels, two counter rotating vortices were generated, one into the MAC region and the other away from it. This counter clockwise vortex, present in all of the rectangular channels, pulled the microparticles into the MAC region and away from being deflected. However, for the half-circular channels, only one strong vortex was dominating the cross-section in the clockwise direction pushing the microparticles in the direction of wave propagation.

4.3. *Acoustofluidic manipulation of microparticles based on travelling surface acoustic wave-induced acoustic radiation force*

When SAWs refract into a microchannel, the transmitted LWs propagate through a fluid medium at the Rayleigh angle and impart either an ARF or ASF-induced drag force [1] on the microparticles suspended in the fluid. The Helmholtz number (κ) has been extensively used to estimate the relative dominance of the ARF and ASF-induced drag force [1,35]. This dimensionless number represents the relative physical dimension of the microparticle with respect to the acoustic wavelength and can be expressed as $\kappa = \pi d_p/\lambda_f = ka$, where d_p is the particle diameter, $\lambda_f\,(=c_f/f)$ is the acoustic wavelength in the fluid at frequency f, $k = 2\pi/\lambda_f$ is the wavenumber, and a is the particle radius [36]. The acoustic scattering can be categorized into Rayleigh ($\kappa \ll 1$), Mie ($\kappa \cong 1$), and Geometrical ($\kappa \gg 1$) scattering regimes [35]. When microspheres, with a diameter comparable to or larger than the acoustic wavelength divided by pi ($d_p \geq \lambda_f/\pi$), suspended in fluid are exposed to progressive LWs, the spherical microparticles scatter the LWs in an anisotropic manner in the Mie or Geometrical scattering regimes. As a consequence, the ARF dominates over the ASF-induced drag force, and the microparticles are translocated in the direction of the wave propagation. The ARF factor (F_F) induced by the SAWs is expressed as $F_F = \langle F\rangle/(\pi d_p^2\bar{E}/4)$, where $\langle F\rangle$ is

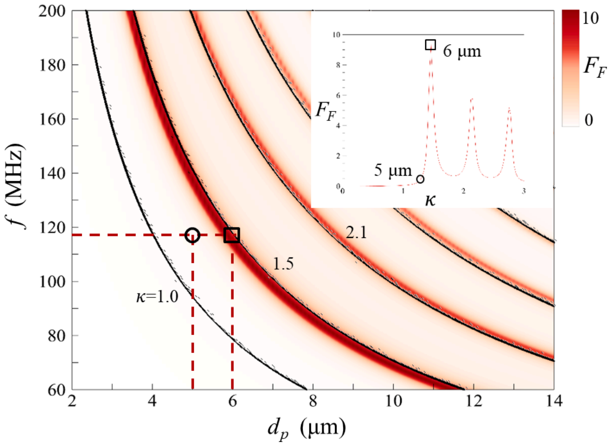

Fig. 5. (a) Contour plot showing the acoustic radiation force factor (F_F) with varying acoustic wave frequency (f) and the PS particle diameter (d_p). Inset (b) F_F is plotted as a function of the Helmholtz number (κ) for a constant frequency $f = 117$ MHz.

a time-averaged ARF and $\bar{E}$ is the mean energy density of the incident wave. The ARF factor acting on the elastic polymer microparticles as a function of κ can be characterized with several maxima peaks and minima valleys, where each peak is attributed to a resonance mode of the freely vibrating elastic microsphere subjected to an oscillating acoustic pressure field, as shown in Fig. 5 [37]. In contrast, the ARF factor acting on the rigid microparticles, such as fused silica, monotonically increases and reach a plateau [38]. For $\kappa < 1$, the microparticles scatter the waves in an isotropic manner (Rayleigh scattering), and the ARF acting on the particles is almost zero in the wave propagation direction. In this work, we have used the fluorescent PS microspheres with diameter of 5 μm (green) and 6 μm (red) under the acoustic field at 117 MHz. As shown in Fig. 5, the elastic PS microspheres experience the most significant acoustic radiation force induced by travelling surface acoustic wave at $\kappa \approx 1.5$ [10,12]. Despite the Mie scattering off both 5 μm ($\kappa \approx 1.25$) and 6 μm ($\kappa \approx 1.5$) PS microspheres, the 6 μm particles experience a relatively higher ARF. The 6 μm particles are deflected more than the 5 μm particles from their original trajectories at the fixed electrical power applied to the transducer, which is validated in the separation experimental results.

We have previously demonstrated sorting of microparticles in the rectangular microchannel by avoiding the MAC region with the help of a sheath flow [5,9,10,39]. Being aware of the possibility of particles being stuck in the MAC region during the sorting process, in this work, we have proposed a residue and MAC-free approach to more efficiently deflect particles and exchange medium around them. Fig. 6 shows acoustofluidic sorting of red fluorescent 6 μm PS microparticles inside rectangular (a-e) and half-circular (f-j) microchannels under the acoustic field at 117 MHz. For stable suspension and minimizing the particle sedimentation in the solution, a biocompatible surfactant TWEEN® 20 was added to the sample fluid. For these sets of the experiments, we used the two inlets and two outlets (without using the inlet 3 in Fig. 1(a)) in the microchannel. The height of the rectangular microchannel at the deflection zone was 57 μm for a range of channel widths (150–500 μm) (Fig. 6(a–e)). The sample fluid was injected into the inlet 1 at a flow rate of 10 μL/h into the microchannel, while the sheath fluid of DI water was introduced into the inlet 2 at a flow rate of 140 μL/h (1:14 sample to sheath flow ratio) to focus the PS carrier microparticles close to the microchannel wall near the SFIT (Fig. 6(b)). The streamlines of the sample particles were unaffected when the SFIT was not activated; therefore, the particles were collected through the outlet 1. Upon actuation of the SFIT by 117 MHz AC signal at 4.2 mW, the SAWs in the direction perpendicular to the flow direction exerted an ARF on the 6 μm PS particles ($\kappa \approx 1.5$) to deflect them in the direction of SAW propagation. A large portion of these particles with a high F_F value were pushed across the laminar flow streamlines to translocate close to the

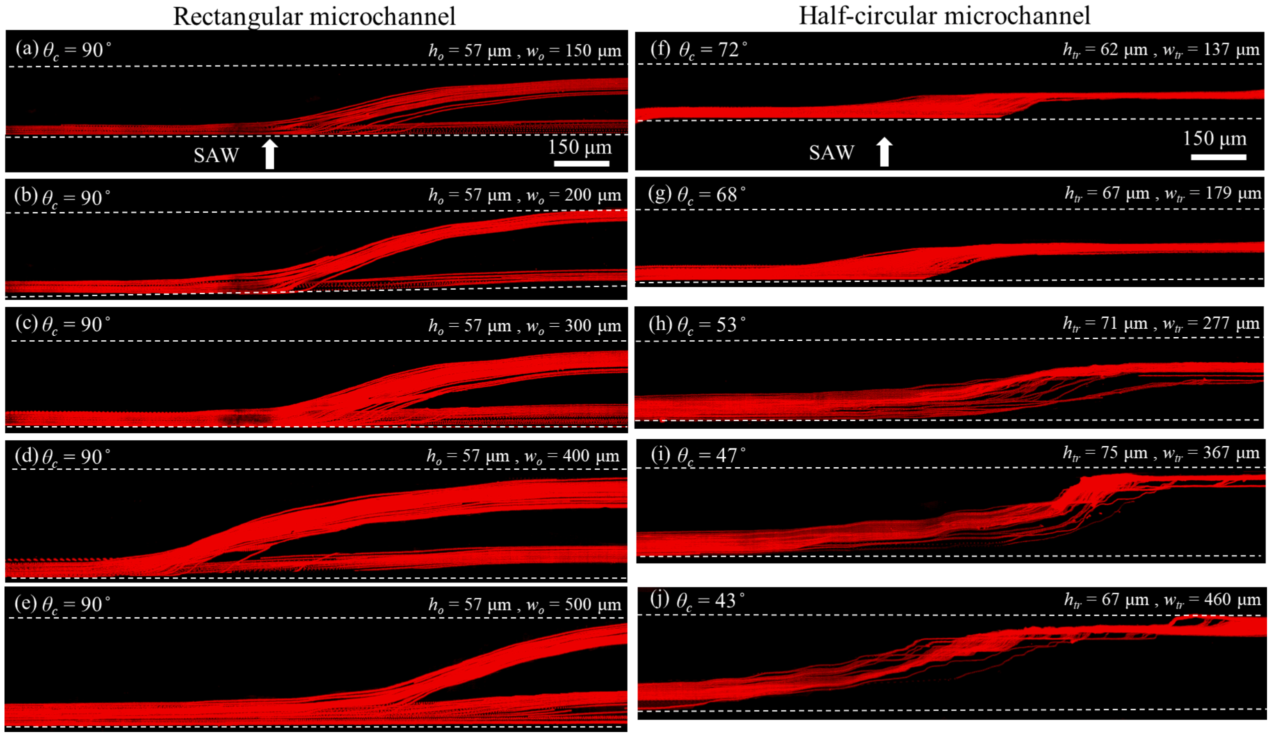

Fig. 6. (a–e) All the rectangular microchannels with $\theta_C = 90^\circ$ show the presence of MAC as a portion of particles flowing past the SAWs unaffected without deflection. (f–j) All the half-circular microchannels with $\theta_C = 43$–72° depict total deflection of the particles across the microchannel width. Half-circular microchannel with θ_C of 68° (f) and 72° (g) show a very smooth particle deflection. However, for θ_C of 53° (h), 47° (i) and 43° (j), formation of straight particle streaks parallel to the channel side edges indicate standing waves formation.

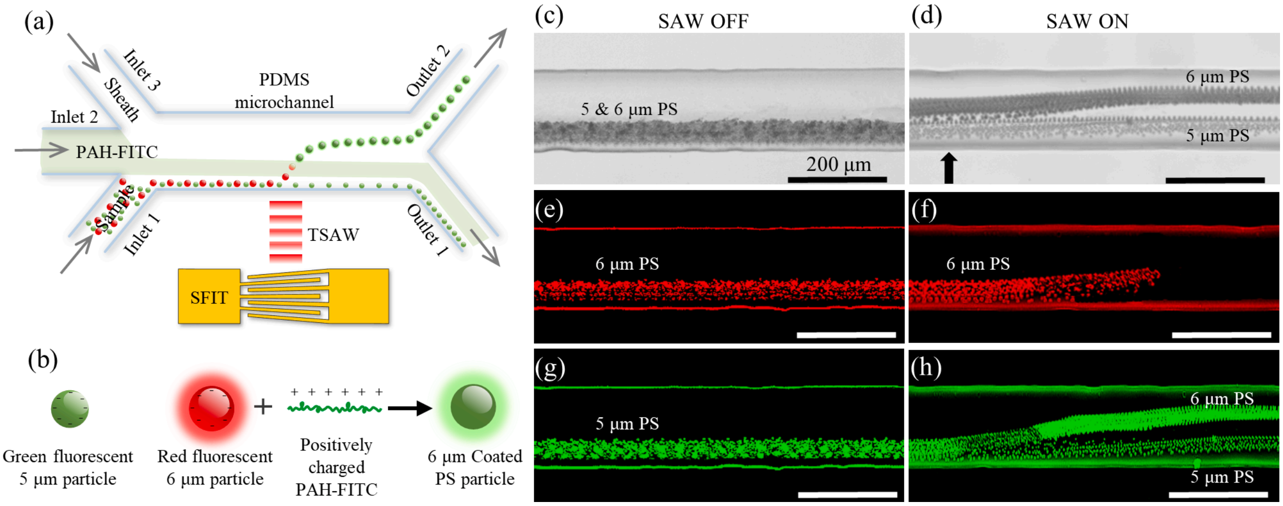

Fig. 7. Size-selective coating of 6 µm negatively charged polystyrene particles. (a) 6 µm red particles are vertically deflected through a fluorescently labeled positively charged PAH–FITC solution (green), while 5 µm green PS particles flow through the channel unaffected. (b) 6 µm red PS particles are chemically coated with the green PAH-FITC molecules. (c–h) Trajectories of the 6 and 5 µm particles with and without the SAW are shown.

microchannel wall opposite to the SFIT, collected through the outlet 2. However, a portion of the particles flowing within the MAC region was not deflected due to the absence of the sufficient ARF and remained as residue particles, collected through the outlet 1. A similar set of experiments were performed in the half-circular channels with varying θ_C of 43–72° to demonstrate residue-free acoustofluidic manipulation of the particles, as shown in Fig. 6(f-j). The half-circular microchannels with θ_C of 72° and 68° showed smooth deflection of particles (Fig. 6(f and g)). All the particles were deflected by the SAW-induced ARF as the corner area was filleted during thermal reflow process, which prevented the formation of a counter-clockwise ASF vortex to pull the particles, while the clockwise ASF vortex brought the particles further under the ARF influence, as in Fig. 4(c and d). In other words, no MAC region was formed in the microchannel. For $\theta_C \leq \theta_R$, the LWs propagating at the Rayleigh angle ($\theta_R = 22°$) were reflected within the half-circular channel to constructively interfere and form standing waves. This interference resulted in the formation of pressure nodes and antinodes across the microchannel, thereby creating a hybrid of travelling and standing acoustic fields. Therefore, we observed that the microparticles were mainly pushed in the wave propagation direction by the SAW-based ARF while some of the particles were also trapped at the acoustic pressure nodes within the channel and temporarily start flowing in a linear manner (Fig. 6(h-j) and Movie 1). For quantitative investigation on the deflection efficiency for the experiments in Fig. 6, we conducted hemocytometer analysis on the collected samples. The concentration of the red fluorescent 6 µm polystyrene microparticles was measured as 5×10^6 particles/mL. The deflection efficiency was calculated as the number of the particles collected at the outlet 2 (collection) out of the total number of the particles collected at the outlets 1 (waste) and 2. The results were (a) 76.3%, (b) 73.3%, (c) 76.6%, (d) 75.1%, (e) 70.1% in the rectangular microchannels, and (f-j) 100% in the half-circular microchannels (see Fig. S1).

4.4. *Acoustofluidic size-selective coating of particles*

In the present study, we separated 6 µm PS particles from 5 µm PS particles for label-free size-selective microparticle coating without any residue target particles, using a half-circular microchannel of h_{tr}, w_{tr} and θ_C of 67 µm, 179 µm and 68°, respectively. We injected the sample solution, including the negatively charged red fluorescent 6 µm and green fluorescent 5 µm PS particles, into the inlet 1 (10 µL/h), a PAH–FITC solution into the inlet 2 (20 µL/h), and a sheath fluid (DI water) into the inlet 3 (50 µL/h) (Fig. 7(a and b)). The concentration of the microparticles was measured as 10^6 particles/mL. Under the SAWs at 117 MHz, the κ-values of the suspended 6 µm (originally red) and 5 µm (green) PS particles were determined to be 1.5 and 1.25, respectively, ensuring that the red particles experienced a strong ARF compared to the green particles. Once the SFIT was actuated at a frequency of 117 MHz the SAWs deflected negatively charged carboxylate functionalized 6 µm red polystyrene particles from their streamlines due to high F_F value ($\kappa > 1$), which were then electrostatically coated with the fluorescently labeled, positively charged PAH–FITC solution and collected at the outlet 2 (Fig. 7(c-h) and Movie 2). Fig. 7(c and d) are bright-field images, Fig. 7(e and f) are red fluorescent images, and Fig. 7(g and h) are green fluorescent images. In the left part of the microchannel in Fig. 7(h), the originally red fluorescent 6 µm particles are not visible by green fluorescent imaging whereas those particles can be identified by red fluorescent imaging as shown in Fig. 7(f). During the migration of 6 µm PS particles from the sample fluid to the sheath fluid passing through the PAH–FITC solution, some microparticles were coated sooner than the others depending on the contact of the PS particles with the PAH–FITC solution. As all the particles passed through the PAH–FITC solution, all of them were found coated, as can be seen in Fig. 7(f and h). Therefore, the red fluorescence signal disappeared eventually as the red fluorescent particles were coated with green fluorescence molecules. The green 5 µm PS particles were collected at the outlet 1 after continuing to flow along their previously focused streamlines without deflection. For clear validation on the residue-free acoustofluidic selective microparticle coating in Fig. 7, we have performed additional experiments with red fluorescent 6 µm and green fluorescent 5 µm PS particles in the half-circular microchannel without the PAH-FITC solution used for the experiments. Fig. S2 shows the hemocytometer images of the red (6 µm) and green (5 µm) microparticles collected at the outlets, where the purity and separation efficiency were measured to be 100% and 97.37%, respectively. The purity was calculated as the number of the target particles (red 6 µm) out of the total number of the particles (red 6 µm and green 5 µm) at the outlet 2 (collection) while the separation efficiency was calculated as the number of the target particles collected at the outlet 2 (collection) out of the number of the target particles collected at the outlet 1 (waste) and 2. The separation efficiency of slightly <100% may have been attributed to the size distribution of the fluorescent microparticles.

The surfaces of the uncoated and coated 6 µm particles were analyzed using SEM images of the PS microparticles in Fig. 8(a–c). The surfaces of the uncoated 6 µm microparticles were smooth, with no evident topography (Fig. 8(b)). The particles collected after being in

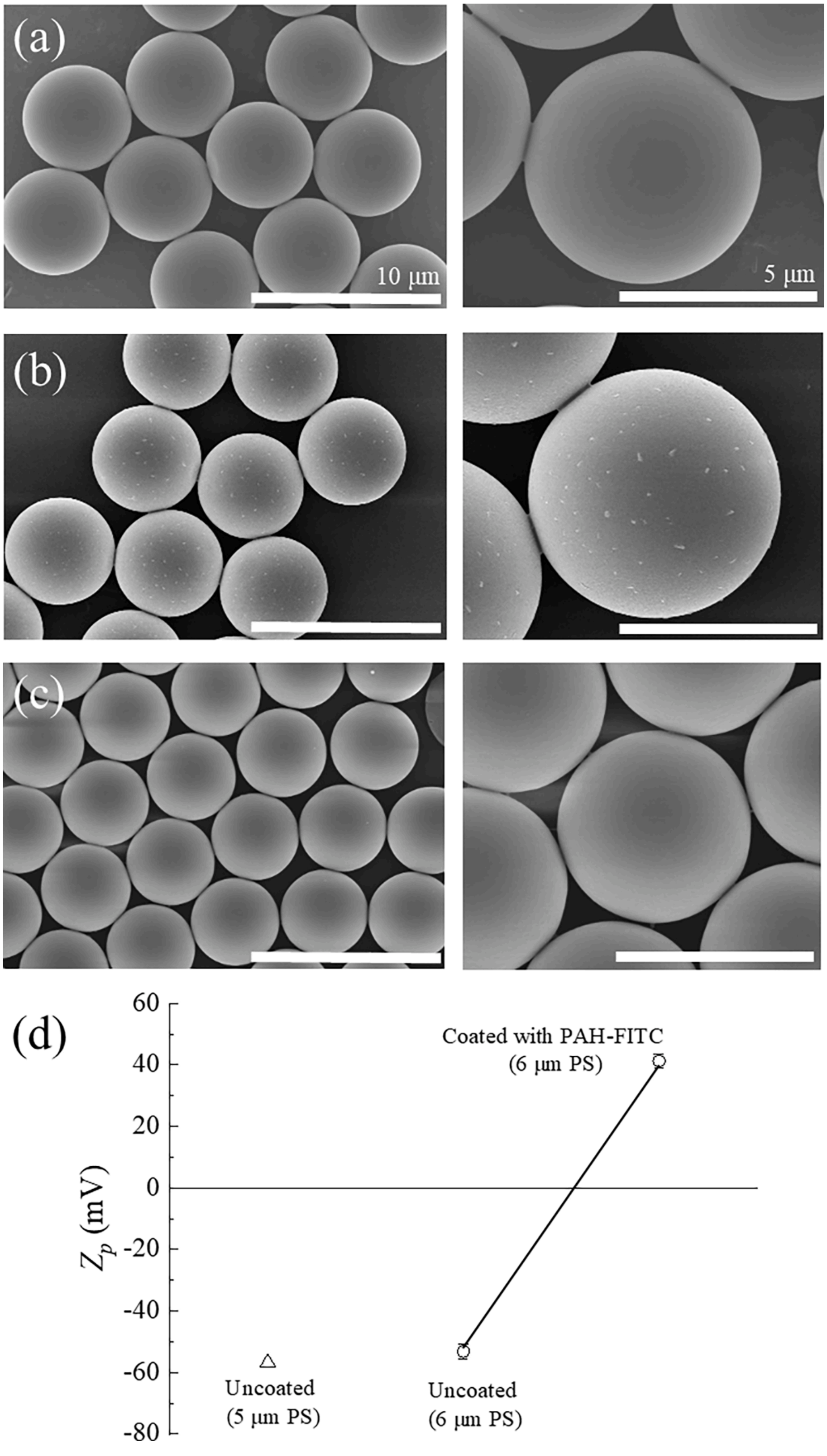

Fig. 8. SEM analysis of (a) the 6 μm uncoated, (b) PAH-FITC 6 μm coated and (c) 5 μm uncoated polystyrene microparticles. (a & c) Uncoated polystyrene particles show smooth surfaces. (b) PAH-FITC coating shows increasing surface roughness compared to the uncoated particles. (d) Zeta potential of uncoated polystyrene (PS) and PAH-FITC coated particles. Error bars represent standard deviation of 5 and 6 μm PS particles measurements.

contact with the PAH–FITC solution, on the other hand, had a rougher surface topology than the uncoated particles, indicating PAH–FITC coating (Fig. 8(b)). Similarly, the surfaces of the uncoated 5 μm microparticles were also smooth, with no evident topography (Fig. 8(c)). The uncoated 5 and 6 μm PS microparticles had zeta potential values of −57.8 mV and −55.8 mV, respectively, whereas the PAH-FITC coated 6 μm polystyrene microparticles had zeta potential values of 42 mV (Fig. 8 (d)). The potential difference between the fluid dispersion medium and the stationary layer of the dispersion medium connected to the dispersed particle is referred to as the zeta potential. In the same suspension medium, a negative zeta potential indicates that the net charge of the scattering particles is negative, as in the case of carboxylate-functionalized PS particles, while a positive value indicates that the particles have a net positive surface charge. The zeta potential's magnitude indicates the degree of electrostatic repulsion between adjacent, similarly charged particles in dispersion. The presence of alternating layers following electrostatic coating of the particles is suggested by the movement of the zeta potential from negative to positive.

5. Conclusions

We developed a SAW-based acoustofluidic device for residue-free microparticle manipulation by the SAW-induced ARF. In the proposed device, a half-circular microchannel fabricated by thermal reflow of the rectangular PR mold was used to remove the MAC region with the optimal $\theta_C = 90^\circ - \theta_R$ of the microchannel. The effects of ARF and ASF were investigated using numerical simulations of the first-order total pressure, time-averaged absolute pressure, ASF body force, and ASF velocity fields. We confirmed the presence of MAC region in the rectangular microchannel and found that the residue particles in the MAC region are attributed to both the deficient acoustic pressure field and the counter clockwise ASF vortex. In the half-circular microchannel-embedded acoustofluidic device without the MAC region, we achieved residue-free microparticle manipulation in a continuous, label-free, and non-contact manner. We utilized the proposed device for residue-free microparticle separation and size-selective fluorescent coating of the microparticles with purity of 100% and separation efficiency of 97.37%.

Declaration of Competing Interest

The authors declare that they have no known competing financial interests or personal relationships that could have appeared to influence the work reported in this paper.

Data availability

Data will be made available on request.

Acknowledgment

This work was supported by the National Research Foundation of Korea (NRF) grant funded by the Korea government (MSIT) (No. 2020R1A5A8018367), a grant of the Korea Health Technology R&D Project through the Korea Health Industry Development Institute (KHIDI), funded by the Ministry of Health & Welfare, Republic of Korea (grant number: HI19C0642), and Nanomedical Devices Development Project of NNFC.

Appendix A. Supplementary data

Supplementary data to this article can be found online at https://doi.org/10.1016/j.ultsonch.2022.106161.

References

[1] G. Destgeer, H.J. Sung, Recent advances in microfluidic actuation and micro-object manipulation via surface acoustic waves, Lab Chip 15 (13) (2015) 2722–2738.

[2] X. Ding, P. Li, S.-C. Lin, Z.S. Stratton, N. Nama, F. Guo, D. Slotcavage, X. Mao, J. Shi, F. Costanzo, T.J. Huang, Surface acoustic wave microfluidics, Lab Chip 13 (18) (2013) 3626.

[3] Y. Gao, M. Wu, Y. Lin, J. Xu, Acoustic microfluidic separation techniques and bioapplications: a review, Micromachines 11 (10) (2020) 921.

[4] D.J. Collins, Z. Ma, J. Han, Y. Ai, Continuous micro-vortex-based nanoparticle manipulation via focused surface acoustic waves, Lab Chip 17 (1) (2017) 91–103.

[5] G. Destgeer, B.H. Ha, J. Park, J.H. Jung, A. Alazzam, H.J. Sung, Microchannel anechoic corner for size-selective separation and medium exchange via traveling surface acoustic waves, Anal. Chem. 87 (9) (2015) 4627–4632.

[6] Y.-C. Li, H.-B. Xin, H.-X. Lei, L.-L. Liu, Y.-Z. Li, Y. Zhang, B.-J. Li, Manipulation and detection of single nanoparticles and biomolecules by a photonic nanojet, Light Sci. Appl. 5 (12) (2016) e16176–e.

[7] X. Ding, S.-C. Lin, B. Kiraly, H. Yue, S. Li, I.-K. Chiang, J. Shi, S.J. Benkovic, T. J. Huang, On-chip manipulation of single microparticles, cells, and organisms using surface acoustic waves, PNAS 109 (28) (2012) 11105–11109.

[8] J. Park, J.H. Jung, G. Destgeer, H. Ahmed, K. Park, H.J. Sung, Acoustothermal tweezer for droplet sorting in a disposable microfluidic chip, Lab Chip 17 (6) (2017) 1031–1040.

[9] H.-D. Xi, H. Zheng, W. Guo, A.M. Gañán-Calvo, Y.e. Ai, C.-W. Tsao, J. Zhou, W. Li, Y. Huang, N.-T. Nguyen, S.H. Tan, Active droplet sorting in microfluidics: a review, Lab Chip 17 (5) (2017) 751–771.

[10] M. Afzal, J. Park, J.S. Jeon, M. Akmal, T.-S. Yoon, H.J. Sung, Acoustofluidic Separation of Proteins Using Aptamer-Functionalized Microparticles, Anal. Chem. 93 (23) (2021) 8309–8317.

[11] L. Mazutis, J. Gilbert, W.L. Ung, D.A. Weitz, A.D. Griffiths, J.A. Heyman, Single-cell analysis and sorting using droplet-based microfluidics, Nat. Protoc. 8 (5) (2013) 870–891.

[12] M. Afzal, J. Park, G. Destgeer, H. Ahmed, S.A. Iqrar, S. Kim, S. Kang, A. Alazzam, T.-S. Yoon, H.J. Sung, Acoustomicrofluidic separation of tardigrades from raw cultures for sample preparation, Zool. J. Linn. Soc. (2019).

[13] H. Ahmed, et al., Surface acoustic wave-based micromixing enhancement using a single interdigital transducer. Appl. Phys. Lett., 2019. 114(4): p. 043702.

[14] Hsu, J.-C. and C.-Y. Chang, Enhanced acoustofluidic mixing in a semicircular microchannel using plate mode coupling in a surface acoustic wave device. Sensors and Actuators A: Physical, 2022. 336: p. 113401.

[15] J. Park, G. Destgeer, M. Afzal, H.J. Sung, Acoustofluidic generation of droplets with tunable chemical concentrations, Lab Chip 20 (21) (2020) 3922–3929.

[16] M. Cecchini, et al., Acoustic-counterflow microfluidics by surface acoustic waves. Appl. Phys. Lett., 2008. 92(10): p. 104103.

[17] M.B. Dentry, J.R. Friend, L.Y. Yeo, Continuous flow actuation between external reservoirs in small-scale devices driven by surface acoustic waves, Lab Chip 14 (4) (2014) 750–758.

[18] Q. Aisha, J.R. Friend, L.Y. Yeo, Investigation of SAW atomization. *2009 IEEE International Ultrasonics Symposium*, 2009.

[19] A. Winkler, S.M. Harazim, S.B. Menzel, H. Schmidt, SAW-based fluid atomization using mass-producible chip devices, Lab Chip 15 (18) (2015) 3793–3799.

[20] H. Afsaneh, R. Mohammadi, Microfluidic platforms for the manipulation of cells and particles, Talanta Open 5 (2022), 100092.

[21] J.-S. Kwon, J.H. Oh, Microfluidic technology for cell manipulation, Appl. Sci. 8 (6) (2018) 992.

[22] G. Destgeer, et al., Characterization of microchannel anechoic corners formed by surface acoustic waves, Appl. Phys. Lett. 112 (2018), 083501.

[23] J. Nam, H. Lim, S. Shin, Manipulation of microparticles using surface acoustic wave in microfluidic systems: a brief review, Korea-Aust. Rheol. J. 23 (4) (2011) 255–267.

[24] M. Wu, A. Ozcelik, J. Rufo, Z. Wang, R. Fang, T. Jun Huang, Acoustofluidic separation of cells and particles, Microsyst. Nanoeng. 5 (1) (2019).

[25] S. Zhao, M. Wu, S. Yang, Y. Wu, Y. Gu, C. Chen, J. Ye, Z. Xie, Z. Tian, H. Bachman, P.-H. Huang, J. Xia, P. Zhang, H. Zhang, T.J. Huang, A disposable acoustofluidic chip for nano/microparticle separation using unidirectional acoustic transducers, Lab Chip 20 (7) (2020) 1298–1308.

[26] H. Ahmed, G. Destgeer, J. Park, J.H. Jung, H.J. Sung, Vertical hydrodynamic focusing and continuous acoustofluidic separation of particles via upward migration, Adv. Sci. 5 (2) (2018) 1700285.

[27] H. Ahmed, G. Destgeer, J. Park, M. Afzal, H.J. Sung, Sheathless focusing and separation of microparticles using tilted-angle traveling surface acoustic waves, Anal. Chem. 90 (14) (2018) 8546–8552.

[28] J. Park, G. Destgeer, H. Kim, Y. Cho, H.J. Sung, In-droplet microparticle washing and enrichment using surface acoustic wave-driven acoustic radiation force, Lab Chip 18 (19) (2018) 2936–2945.

[29] R. Kirchner, H. Schift, Thermal reflow of polymers for innovative and smart 3D structures: A review, Mater. Sci. Semicond. Process. 92 (2019) 58–72.

[30] O.M. Ikumapayi, et al., Microfabrication and nanotechnology in manufacturing system – An overview, Mater. Today:. Proc. 44 (2021) 1154–1162.

[31] D.J. Collins, Z. Ma, Y. Ai, Highly localized acoustic streaming and size-selective submicrometer particle concentration using high frequency microscale focused acoustic Fields, Anal. Chem. 88 (10) (2016) 5513–5522.

[32] C. Devendran, T. Albrecht, J. Brenker, T. Alan, A. Neild, The importance of travelling wave components in standing surface acoustic wave (SSAW) systems, Lab Chip 16 (19) (2016) 3756–3766.

[33] F. Kiebert, S. Wege, J. Massing, J. König, C. Cierpka, R. Weser, H. Schmidt, 3D measurement and simulation of surface acoustic wave driven fluid motion: a comparison, Lab Chip 17 (12) (2017) 2104–2114.
[34] S. Shiokawa, Y. Matsui, The dynamics of SAW streaming and its application to fluid devices, MRS Online Proceed. Library 360 (1) (1994) 53–64.
[35] M.A.S. Pessôa, A.A.R. Neves, Acoustic scattering and forces on an arbitrarily sized fluid sphere by a general acoustic field, J. Sound Vib. 479 (2020), 115373.
[36] G. Destgeer, B.H. Ha, J.H. Jung, H.J. Sung, Submicron separation of microspheres via travelling surface acoustic waves, Lab Chip 14 (24) (2014) 4665–4672.
[37] T. Hasegawa, K. Yosioka, Acoustic-radiation force on a solid elastic sphere, J. Acoust. Soc. Am. 46 (5B) (1969) 1139–1143.
[38] G. Destgeer, J.H. Jung, J. Park, H. Ahmed, K. Park, R. Ahmad, H.J. Sung, Acoustic impedance-based manipulation of elastic microspheres using travelling surface acoustic waves, RSC Adv. 7 (36) (2017) 22524–22530.
[39] C. Wyatt Shields IV, C.D. Reyes, G.P. López, Microfluidic cell sorting: a review of the advances in the separation of cells from debulking to rare cell isolation, Lab Chip 15 (5) (2015) 1230–1249.